

# Active spintronic-metasurface terahertz emitters with tunable chirality

Changqin Liu,<sup>a,b,†</sup> Shunjia Wang<sup>✉,a,†</sup> Sheng Zhang,<sup>a,†</sup> Qingnan Cai,<sup>a,†</sup> Peng Wang,<sup>a</sup> Chuanshan Tian,<sup>a</sup> Lei Zhou,<sup>a,\*</sup> Yizheng Wu,<sup>a,b,\*</sup> and Zhensheng Tao<sup>a,\*</sup>

<sup>a</sup>Fudan University, Department of Physics and State Key Laboratory of Surface Physics, Shanghai, China

<sup>b</sup>Shanghai Research Center for Quantum Sciences, Shanghai, China

**Abstract.** The ability to generate and manipulate broadband chiral terahertz waves is essential for applications in material imaging, terahertz sensing, and diagnosis. It can also open up new possibilities for nonlinear terahertz spectroscopy and coherent control of chiral molecules and magnetic materials. The existing methods, however, often suffer from low efficiency, narrow bandwidth, or poor flexibility. Here, we propose a novel type of laser-driven terahertz emitters, consisting of metasurface-patterned magnetic multilayer heterostructures, that can overcome the shortcomings of the conventional approaches. Such hybrid terahertz emitters combine the advantages of spintronic emitters for being ultrabroadband, efficient, and highly flexible, as well as those of metasurfaces for the powerful control capabilities over the polarization state of emitted terahertz waves on an ultracompact platform. Taking a stripe-patterned metasurface as an example, we demonstrate the efficient generation and manipulation of broadband chiral terahertz waves. The ellipticity can reach  $>0.75$  over a broad terahertz bandwidth (1 to 5 THz), representing a high-quality and efficient source for few-cycle circularly polarized terahertz pulses with stable carrier waveforms. Flexible control of ellipticity and helicity is also demonstrated with our systematic experiments and numerical simulations. We show that the terahertz polarization state is dictated by the interplay between laser-induced spintronic-origin currents and the screening charges/currents in the metasurfaces, which exhibits tailored anisotropic properties due to the predesigned geometric confinement effects. Our work opens a new pathway to metasurface-tailored spintronic emitters for efficient vector-control of electromagnetic waves in the terahertz regime.

Keywords: chiral terahertz generation; active metasurface; time-domain terahertz; spectroscopy.

Received Jul. 16, 2021; revised manuscript received Sep. 9, 2021; accepted for publication Sep. 29, 2021; published online Oct. 25, 2021.

© The Authors. Published by SPIE and CLP under a Creative Commons Attribution 4.0 International License. Distribution or reproduction of this work in whole or in part requires full attribution of the original publication, including its DOI.

[DOI: [10.1117/1.AP.3.5.056002](https://doi.org/10.1117/1.AP.3.5.056002)]

## 1 Introduction

Coherent terahertz sources driven by femtosecond laser pulses can now routinely generate sub-picosecond few-cycle terahertz waves with exceptionally stable carrier waveforms, which can be used in numerous fundamental studies and practical applications.<sup>1,2</sup> The ability to manipulate the three-dimensional (3D) electric-field vector of such broadband terahertz waveforms can substantially broaden the applications of the terahertz technologies and open up new possibilities for studies of coherent

light–matter interactions,<sup>3–6</sup> as well as of novel ultrafast quantum control facilitated by phase-stable strong terahertz fields.<sup>7–9</sup> Therefore, a great amount of research has been devoted to generating chiral terahertz waves and realizing full control over the 3D field-vectors in their amplitude, phase, frequency, polarization, and spatial properties. Hitherto, the existing methods can be categorized into: (1) direct generation from gas plasmas, e.g., by applying external fields<sup>10–13</sup> or a combined two-color laser scheme,<sup>14,15</sup> but these methods are only applicable for high-energy mJ-level laser amplifiers; (2) special frequency-conversion techniques in nonlinear crystals,<sup>16,17</sup> magnetic,<sup>18</sup> and novel topological materials,<sup>19,20</sup> yet the generation efficiency is usually low; and (3) implementation of passive optical components, such as terahertz polarizers<sup>21</sup> and waveplates,<sup>22,23</sup> yet they are often

\*Address all correspondence to Lei Zhou, [phzhou@fudan.edu.cn](mailto:phzhou@fudan.edu.cn); Yizheng Wu, [wuyizheng@fudan.edu.cn](mailto:wuyizheng@fudan.edu.cn); Zhensheng Tao, [zhenshengtao@fudan.edu.cn](mailto:zhenshengtao@fudan.edu.cn)

<sup>†</sup>These authors contributed equally to this work.

limited to narrow bandwidth. So, it still attracts great interest to develop a flexible and robust solution for the efficient generation of broadband chiral terahertz waves.

Metasurfaces, two-dimensional (2D) metamaterials composed by subwavelength planar micro-structures (e.g., “meta-atoms”) with tailored electromagnetic responses, have greatly enriched our capability of wave manipulation in the terahertz regime.<sup>24–29</sup> By engineering the electromagnetic properties of individual meta-atoms and the collective coupling between them, metasurfaces can precisely control the field transformation and achieve predesigned functionalities.<sup>30–32</sup> However, functional meta-devices so far achieved in the terahertz regime are mostly separated from the generation source, which makes it difficult to make the entire device compact. Therefore, it would be extremely attractive if we can combine the state-of-the-art broadband terahertz emitters with metasurface technologies, which could give rise to compact and flexible terahertz sources with full access to waveform control.<sup>33–35</sup>

This, in fact, can be realized by employing the novel spintronic terahertz emitters composed of magnetic multilayer heterostructures.<sup>36–41</sup> These spintronic emitters exhibit the advantages of being low-cost, highly reliable, efficient, and flexible, allowing implementations with a wide range of driving laser conditions, from nJ pulse energy of a compact laser oscillator<sup>36</sup> to mJ pulses delivered by a laser amplifier.<sup>38,42</sup> An ultra-broad spectral bandwidth covering 1 to 30 THz can be produced when excited by short 10-fs laser pulses.<sup>36</sup> Moreover, because the micro-nano fabrication of metal thin films is technologically well established, these spintronic emitters can be easily made into various metasurface structures, opening up great potential for applications. When excited by femtosecond laser pulses, the laser-induced transient currents, which are inherent to the spintronic emitters,<sup>37</sup> can serve as efficient and active driving sources of the metasurface, the properties of which can be well controlled by the excitation lasers and external fields. Hence, such a hybrid terahertz emitter has the potential for high-efficiency terahertz-wave generation and manipulation in a single device. Understanding the influence of the metasurface structure on the laser-induced charge and current dynamics on the microscopic scale is the key for sophisticated device design in the future.

In this work, we propose a novel spintronic-metasurface terahertz emitter, consisting of metasurface-patterned ferromagnetic (FM) and nonmagnetic (NM) heterostructures. Taking the prototypical stripe-pattern metasurface as an example, we demonstrate the generation and manipulation of chiral terahertz waveforms in an efficient and highly flexible manner. The ellipticity can reach  $>0.75$  for a broad terahertz bandwidth (1 to 5 THz), and the generation efficiency is comparable to the nonlinear crystals commercially available. Furthermore, by simply varying the transient spintronic-origin currents with an orientated external magnetic field, the emitter functionality can be actively controlled, leading to continuous tuning of the terahertz polarization state and helicity. We show that the geometric confinement in metallic microstructures can generate anisotropic screening charges/currents in responses to the laser-induced spintronic-origin currents, which, in turn, strongly modifies the polarization characteristics of the terahertz waves emitted from the whole device in the desirable way. Our work opens a new pathway to active metasurface-tailored spintronic devices for efficient generation and control over the electric-field vectors in the terahertz regime.

## 2 Principles and Methods

Figure 1(a) shows the schematic of the experimental setup. In our experiments, the ultrashort laser pulses (duration  $\sim 24$  fs, center wavelength 1030 nm, and repetition rate 100 kHz) generated by a compressed Yb:KGW laser amplifier are used to excite the active spintronic-metasurface device. The high-quality pulse compression is enabled by solitary beam propagation in periodic layered Kerr media.<sup>43</sup> The excitation pulse energy is  $\sim 20 \mu\text{J}$ , and the beam radius on the metasurface emitter is  $\sim 1.1$  mm (see Sec. S1 in the [Supplementary Material](#) for details on the experimental setup). The metasurface emitter is composed of stripe-patterned FM/NM heterostructures. The FM/NM heterostructure consists of NM Pt (thickness of 3 nm) capped with FM  $\text{Fe}_{50}\text{Co}_{50}$  (1.4 nm) and supported by a thick  $\text{SiO}_2$  or  $\text{Al}_2\text{O}_3$  substrate. We note that other FM metals and alloys, such as Fe, Co, and Co-Fe-B alloys, can also be used in substitution for  $\text{Fe}_{50}\text{Co}_{50}$  since similar terahertz signals can be generated from the heterostructures composed of these materials.<sup>36</sup> The stripe patterns are then fabricated by the standard optical lithography and ion beam etching process (see Sec. S2 in the [Supplementary Material](#)). The metasurface structures with different stripe widths ( $d$ ) and spacings ( $l$ ), as well as on different substrates ( $\text{SiO}_2$ ,  $\text{Al}_2\text{O}_3$ ), are investigated [see Fig. 1(a)]. In the experiments, the stripe orientation is fixed along the  $x$  axis, while the magnetization of the FM layer ( $\mathbf{M}$ ) is saturated by an oriented external magnetic field ( $\mathbf{H}$ ) with a field magnitude of 200 mT, and the field orientation can be continuously adjusted in the  $xy$  plane. The field angle  $\theta_H$  is defined as the angle between  $\mathbf{H}$  and the stripe orientation ( $x$  axis), as shown in Fig. 1(a). The applied field is much stronger than the anisotropy field of the FM film, thus the FM magnetization is expected to always align parallel to  $\mathbf{H}$  (see Sec. S3 in the [Supplementary Material](#)). Under femtosecond laser illumination, the longitudinal spin current ( $\mathbf{j}_s$ ) arising in the FM layer is converted into a transverse charge current ( $\mathbf{j}_c$ ) via the inverse spin-Hall effect (ISHE) in the NM layer, given by  $\mathbf{j}_c = \gamma \mathbf{j}_s \times \mathbf{M}/|\mathbf{M}|$ , where  $\gamma$  is the spin-Hall angle of the NM layer.<sup>37</sup> As a result, in our experiments, the laser-induced charge current  $\mathbf{j}_c$  always flows perpendicularly to  $\mathbf{H}$  and serves as an active driving source of the stripe-patterned metasurface [see Fig. 1(a)]. The emitted terahertz field and its polarization state are then detected by the polarization- and time-resolved terahertz spectroscopy setup based on electro-optic sampling (EOS)<sup>44–46</sup> (see Sec. S4 in the [Supplementary Material](#)).

## 3 Results

We first present evidence showing that the metasurface can influence the device functionality by inducing strong amplitude and phase modulations onto the emitted terahertz waveforms. The EOS signals for the terahertz-wave components polarized parallel ( $E^{\parallel}$ ) and perpendicular ( $E^{\perp}$ ) to the stripes are plotted in Fig. 2(a). Clearly, the perpendicular electric-field amplitude  $E^{\perp}$  is strongly suppressed compared to  $E^{\parallel}$ , which is consistent with previous work.<sup>38,47</sup> The results of the peak-to-peak amplitude  $V_{pp}$  [see Figs. 2(a) and 2(b)] as a function of  $\theta_H$  are summarized in Fig. 2(c). The results of both  $E^{\perp}$  and  $E^{\parallel}$  exhibit a sinusoidal behavior, while a  $\sim 90$  deg angle shift can be observed. Furthermore, our results in Figs. 2(a) and 2(b) show that the terahertz waveforms, respectively, for the two orthogonal polarizations, possess almost identical temporal waveforms. This conclusion is further corroborated by the normalized spectra

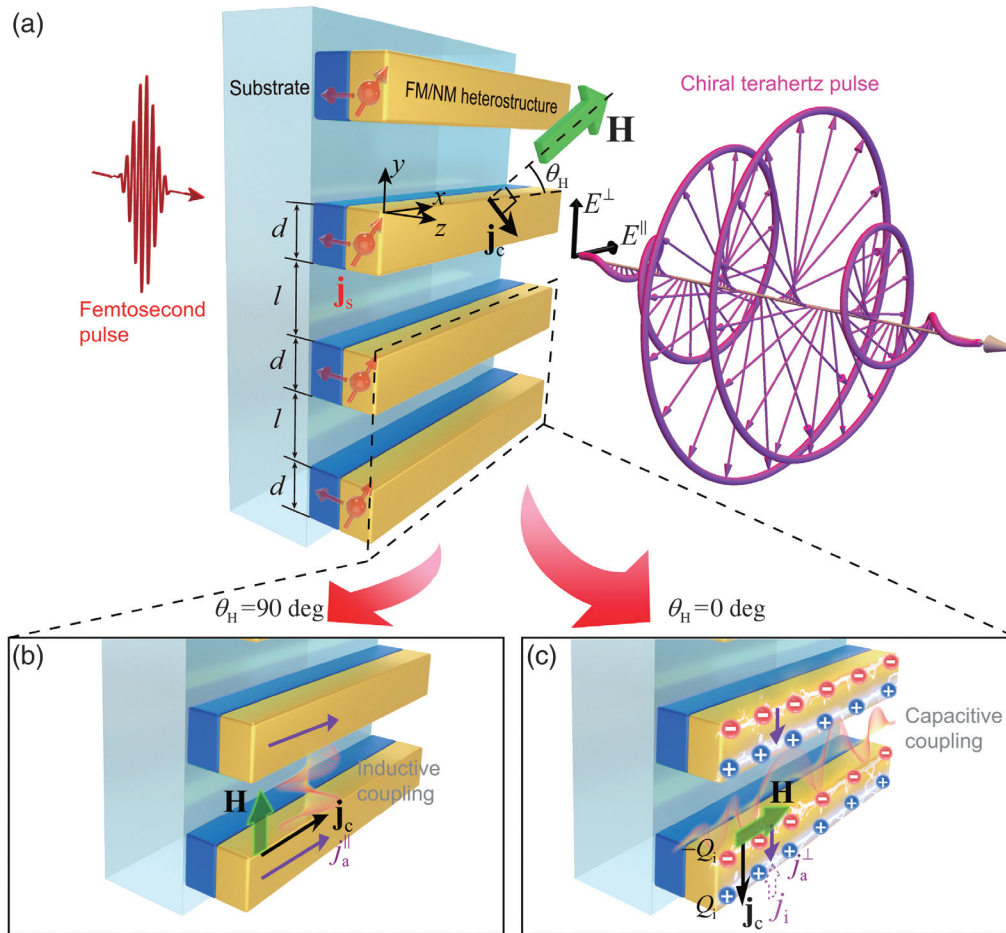


**Fig. 1** Generation of chiral terahertz waves from a stripe-patterned spintronic-metasurface emitter. (a) Schematic of the experimental setup. The femtosecond pulse is focused to excite a stripe-patterned spintronic-metasurface emitter along the  $z$  direction. The stripe is aligned along the  $x$  direction. An orientated external magnetic field ( $\mathbf{H}$ ) is applied in the  $x$ - $y$  plane with a field angle of  $\theta_H$ . A few-cycle chiral terahertz pulse is generated, which can be decomposed into electric-field components parallel ( $E^{\parallel}$ ) and perpendicularly ( $E^{\perp}$ ) to the stripes. The stripe width is  $d$ , and the spacing between the stripes is  $l$ . Under laser illumination, spin currents  $\mathbf{j}_s$  are driven from the FM layer (yellow) to the NM layer (blue) through the interface. (b) Illustration of the current dynamics and inductive coupling in the  $x$ - $y$  plane when  $\theta_H = 90$  deg. Owing to ISHE, spin currents are converted to charge currents  $\mathbf{j}_c$ , which flow along the stripes. (c) Illustration of the charge and current dynamics and the capacitive coupling in the  $x$ - $y$  plane when  $\theta_H = 0$  deg.  $\mathbf{j}_c$  flows perpendicularly to the stripes, which induces the transient charges ( $Q_i$ ) and counteractive currents ( $\mathbf{j}_i$ ), which suppresses the current density  $j_a^{\perp}$ .

shown in Fig. 2(d), which displays identical spectral shapes for each polarization, although the spectrum of  $E^{\perp}$  is blue-shifted compared to  $E^{\parallel}$ .<sup>38,47</sup> The coherent detection of EOS allows us to retrieve the phase information, and, most interestingly, the phase difference ( $\varphi^{\perp} - \varphi^{\parallel}$ ) stays close to  $\pm\pi/2$  throughout the entire spectrum [see Fig. 2(e)]. This clearly indicates the generation of chiral terahertz waves. It is worthy to note that the above results are obtained from a device with  $d = 5 \mu\text{m}$ , and the filling factor (FF)  $d/(d + l) = 0.5$  on a  $\text{SiO}_2$  substrate. Similar observations can be made on other metasurface geometries (see Sec. S5–S7 in the [Supplementary Material](#)).

Our findings here are distinct from past works, which only focused on the amplitude modulation and the spectral shift of the terahertz waves from the stripe-patterned terahertz emitters.<sup>38,47</sup>

Instead, our results clearly show that the directions parallel and perpendicular to the stripes define a set of canonical coordinates, in which the terahertz waveforms of  $E^{\parallel}$  and  $E^{\perp}$  are decoupled from each other and possess a broadband quarter-wave phase difference. This is the key for the generation and manipulation of the chiral terahertz waves.

The above observations can be conceptually captured by a geometric-confinement model, which considers the dynamics and the interplay of the spintronic-origin current density ( $\mathbf{j}_c$ ), as well as the transient metasurface-induced charges ( $Q_i$ ) and current density ( $\mathbf{j}_i$ ) that flows in the  $y$  direction [see Figs. 1(b) and 1(c)]. According to Ohm's law, the complex electric-field component  $E^{\parallel}$  ( $E^{\perp}$ ) of the emitted terahertz wave is proportional to the complex magnitude of the total current density

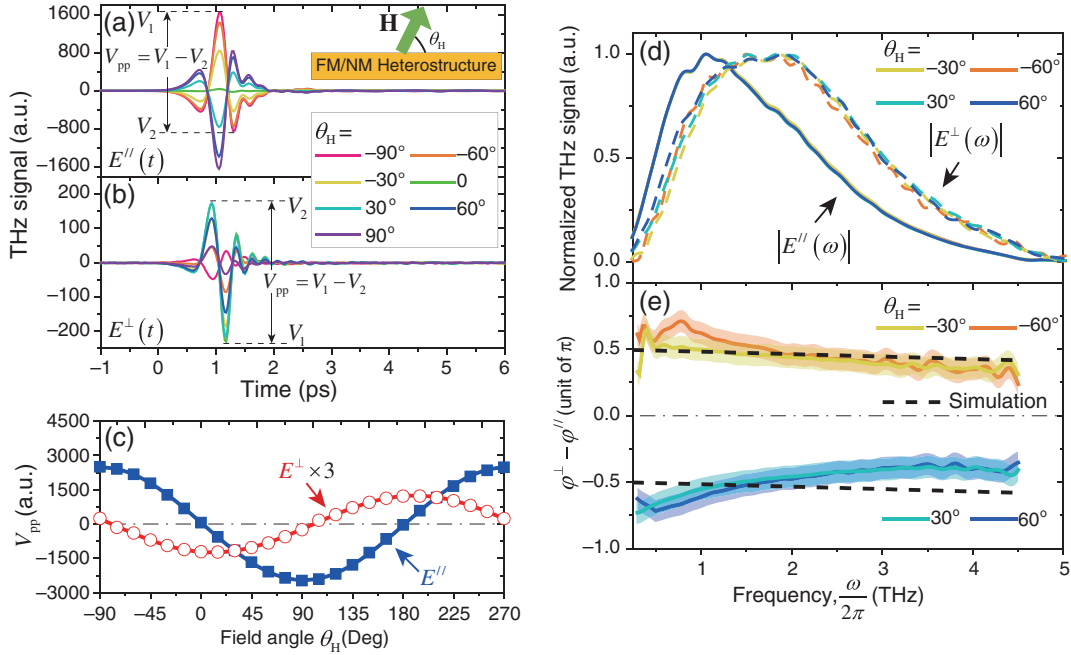


**Fig. 2** Modulation of terahertz spectrum and phase due to metasurface structure. (a) Terahertz waveforms of  $E^{\parallel}$  under different field angles  $\theta_H$ . The peak-to-peak field amplitude ( $V_{pp}$ ) is defined as  $V_1 - V_2$ . (b) Same as (a) for  $E^{\perp}$ . (c) The peak-to-peak field amplitude ( $V_{pp}$ ) of  $E^{\parallel}$  and  $E^{\perp}$  [defined in (a) and (b)] as a function of  $\theta_H$ . (d) Normalized spectra of  $E^{\parallel}$  and  $E^{\perp}$  under different field angles  $\theta_H$ . (e) The relative phase difference between the parallel and the perpendicular components  $\varphi^{\perp} - \varphi^{\parallel}$  under different field angles  $\theta_H$ . The colored regions represent the experimental errors.

flowing in the same direction  $j_a^{\parallel}$  ( $j_a^{\perp}$ ) by  $E^{\parallel}(\omega) = \kappa^{\parallel}(\omega)j_a^{\parallel}(\omega)$  and  $E^{\perp}(\omega) = -\kappa^{\perp}(\omega)j_a^{\perp}(\omega)$ ,<sup>36,37</sup> where  $\kappa^{\parallel,\perp}$  is the proportionality constant which is determined by the conductance of the metal layer and the metasurface geometry, and the minus sign for the perpendicular direction results from our measurement geometry [see Fig. 1(c)]. As shown in Fig. 1(c), along the stripes ( $x$  axis), the current density  $j_a^{\parallel}$  is solely contributed by the  $x$ -component of  $\mathbf{j}_c$ , given by  $j_a^{\parallel} = j_c \sin \theta_H$ , where  $j_c$  represents the complex magnitude of  $\mathbf{j}_c$ . On the other hand, in the direction perpendicular to the stripes ( $y$  axis), the current density  $j_a^{\perp}$  consists of both the  $y$  component of  $\mathbf{j}_c$  and the metasurface-induced “counteractive” current  $j_i$ , which yields  $j_a^{\perp} = j_c \cos \theta_H - j_i$  [see Fig. 1(c)]. The counteractive current  $j_i$  is driven by the electric field built up by the transient charge density  $Q_i$  at the stripe boundaries with  $j_i = \sigma Q_i / C$ , where  $\sigma$  is the metal-layer conductivity, and  $C$  is the constant of proportionality between the charge-induced electric field in the metal layer and the charge density (see Sec. S8 in the [Supplementary Material](#)). Here,  $Q_i$  can be considered as the result of the accretion of  $j_a^{\perp}$  at the stripe boundaries. In the frequency domain, we derive that  $j_i(\omega) = -\frac{\sigma(\omega)}{i\omega C} j_a^{\perp}(\omega)$ . For convenience of discussion, we further assume the low-frequency limit ( $\omega \rightarrow 0$ ), where  $\sigma$  and  $\kappa^{\parallel,\perp}$  both become constant,<sup>48</sup> and it finally yields  $E^{\parallel}(\omega) = \kappa^{\parallel} j_c(\omega) \sin \theta_H$  and  $E^{\perp}(\omega) = -\frac{i\omega\kappa^{\perp}C}{\sigma} j_c(\omega) \cos \theta_H$  (see Sec. S8 in the [Supplementary Material](#) for the detailed derivation). Here, the low-frequency limit corresponds to the terahertz frequency, where the wavelength is much longer than the geometrical period ( $d + l$ ) of the metasurface.

First of all, we obtain from the above model that the amplitude of  $E^{\perp}$  is scaled by a factor of  $\omega\kappa^{\perp}C/\sigma\kappa^{\parallel}$  ( $\omega \rightarrow 0$ ) when compared to  $E^{\parallel}$ , which leads to the observed suppression of  $E^{\perp}$  [see Figs. 2(a) and 2(b)]. The factor of  $\omega$  also explains the spectral blueshift of  $E^{\perp}$  with respect to  $E^{\parallel}$  [see Fig. 2(d)]. Second, the amplitudes of  $E^{\parallel}$  and  $E^{\perp}$  follow the sine- and cosine-functions of  $\theta_H$ , respectively, which is consistent with Fig. 2(c). Finally, the complex amplitudes of  $E^{\parallel}$  and  $E^{\perp}$  exhibit a spectral quarter-wave phase difference, which also agrees with the experimental results in Fig. 2(e). We note that, although this simple model can qualitatively explain the general features of our observations, the quantitative agreement over the entire spectrum is elusive. Neither is the inductive and capacitive coupling of the transient currents and charges between the stripes considered in this model. Hence, numerical simulations using the frequency-domain solver of COMSOL Multiphysics<sup>49</sup> are further conducted to provide a comprehensive understanding of our results and to extract the microscopic mechanism (see Sec. S10 in the [Supplementary Material](#)).

The broadband quarter-wave phase difference naturally leads to chiral terahertz emission. In Fig. 3(a), we plot a typical time dependence of the electric-field vector for a chiral terahertz waveform obtained in our experiments, with the three projections displaying the waveforms of the mutually orthogonal components  $E^{\parallel}(t)$  and  $E^{\perp}(t)$ , and their parametric plot. Here, a stripe pattern with  $d = 10 \mu\text{m}$  and  $\text{FF} = 0.5$  is excited by the laser pulses under  $\theta_H = -17^\circ$ . The generation of the chiral terahertz waveforms can be well captured by our numerical simulation performed for the same device and the same excitation conditions [see Fig. 3(a)]. As clearly shown in Fig. 3(b), the

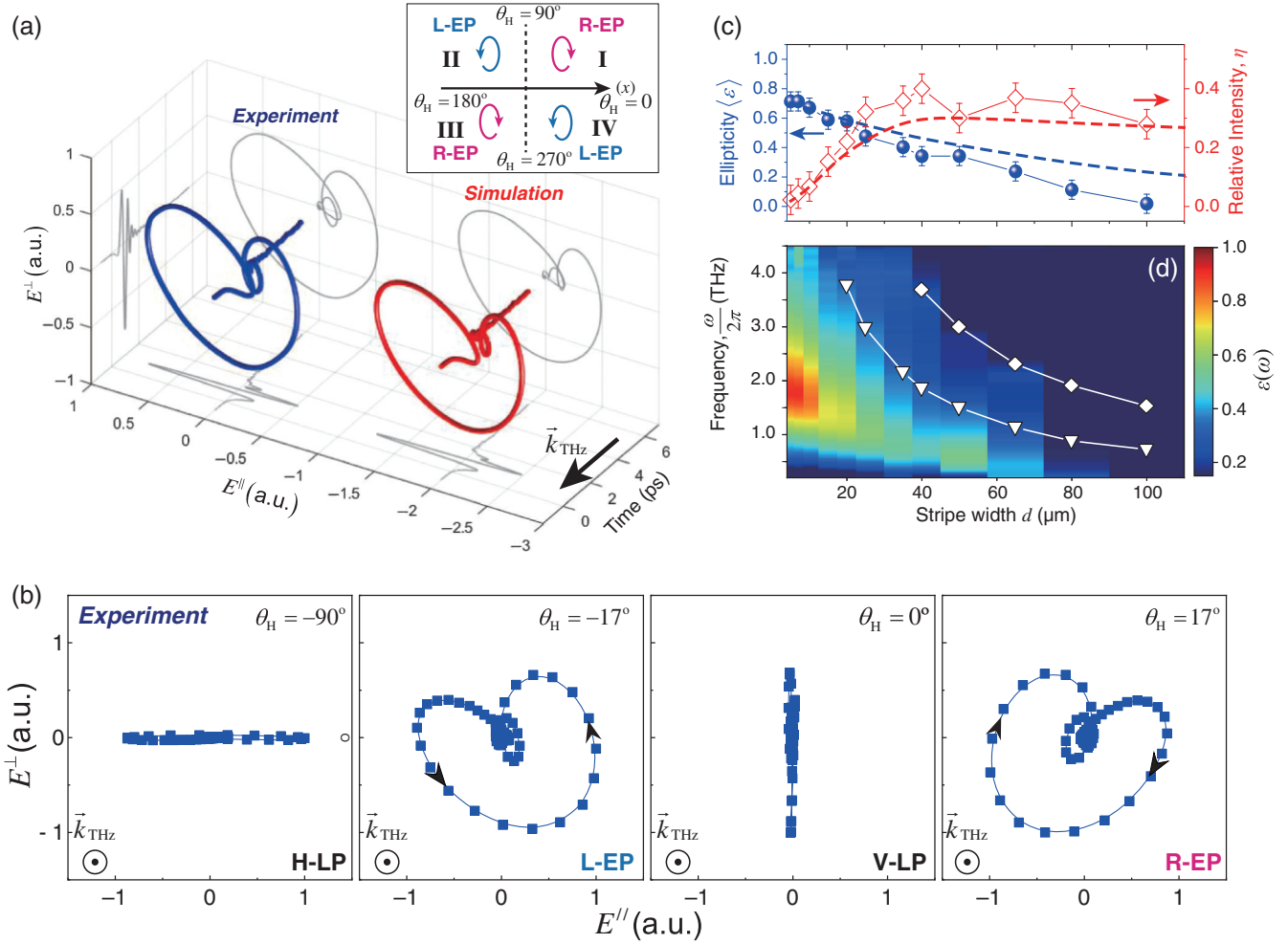


**Fig. 3** Generation and manipulation of chiral terahertz waveforms. (a) Typical time dependence of the electric-field vector for a chiral terahertz waveform generated from a metasurface emitter with  $d = l = 10 \mu\text{m}$  at  $\theta_H = -17$  deg. The simulation result under the same conditions is plotted for comparison. The terahertz wavevector  $\vec{k}_{\text{THz}}$  is labeled. Inset: the illustration of the polarization states under different  $\theta_H$ . L-EP: left-handed elliptical polarization; R-EP: right-handed elliptical polarization. (b) The parametric plots of  $E^{\parallel}(t)$  and  $E^{\perp}(t)$  with different  $\theta_H$  for  $d = l = 10 \mu\text{m}$  under different  $\theta_H$ . H-LP: horizontal linear polarization; V-LP: vertical linear polarization. The direction of  $\vec{k}_{\text{THz}}$  is labeled. (c) The broadband ellipticity  $\langle \epsilon \rangle$  and the relative intensity  $\eta$  for the chiral terahertz waves generated with different stripe width  $d$ . (d) The spectrally resolved ellipticity  $\epsilon(\omega)$  as a function of  $d$ . The white filled symbols represent the anomaly frequencies shown in Fig. 4(e).

ellipticity and handedness of the emitted terahertz radiation can be conveniently and continuously controlled by changing the field angle  $\theta_H$ . These results can also be well reproduced by the simulations (see Fig. S14 in the [Supplementary Material](#)).

To quantitatively characterize the polarization state of the emitted terahertz waveform, the broadband ellipticity  $\langle \epsilon \rangle$  is calculated by considering the spectral intensity and the phase difference over the entire spectrum,

$$\langle \epsilon \rangle = \frac{\int_0^\infty \epsilon(\omega) [ |E^{\parallel}(\omega)|^2 + |E^{\perp}(\omega)|^2 ] d\omega}{\int_0^\infty [ |E^{\parallel}(\omega)|^2 + |E^{\perp}(\omega)|^2 ] d\omega}, \quad (1)$$

and  $\epsilon$  is given as<sup>50,51</sup>

$$\epsilon = \text{sgn}[s_3] \times \sqrt{\frac{|E^{\parallel}|^2 + |E^{\perp}|^2 - \sqrt{(|E^{\parallel}|^2 - |E^{\perp}|^2)^2 + 4|E^{\parallel}|^2|E^{\perp}|^2 \cos^2(\varphi^{\perp} - \varphi^{\parallel})}}{|E^{\parallel}|^2 + |E^{\perp}|^2 + \sqrt{(|E^{\parallel}|^2 - |E^{\perp}|^2)^2 + 4|E^{\parallel}|^2|E^{\perp}|^2 \cos^2(\varphi^{\perp} - \varphi^{\parallel})}}} \quad (2)$$

which can be derived from the Stokes parameters,  $s_3 = 2|E^{\parallel}||E^{\perp}|\sin(\varphi^{\perp} - \varphi^{\parallel})$ <sup>50</sup> (see Sec. S11 in the [Supplementary Material](#)), and  $\epsilon = 1$  and  $-1$  represent left and right circular polarization, respectively, defined from the point of view of the receiver. Because the value of  $\cos^2(\varphi^{\perp} - \varphi^{\parallel})$  over the entire spectrum is almost independent of  $\theta_H$  under a given metasurface structure [Fig. 2(e)], the tuning of the field ellipticity here is realized by adjusting the relative amplitudes of  $E^{\parallel}$  and  $E^{\perp}$  with the field angle  $\theta_H$  according to Eqs. (1) and (2) [see Fig. 2(c)]. The

handedness of the terahertz field, on the other hand, is changed in different regions of the field angle, as illustrated in the inset of Fig. 3(a).

In Fig. 3(c), we summarize the experimental results obtained from the devices with FF = 0.5 of the optimum  $\langle \epsilon \rangle$ , accompanied by the relative intensity  $\eta$  of the terahertz fields. Here,  $\eta$  is given as

$$\eta = \frac{\int_0^\infty [ |E^{\parallel}(\omega)|^2 + |E^{\perp}(\omega)|^2 ] d\omega}{\int_0^\infty |E_{\text{homo}}(\omega)|^2 d\omega}, \quad (3)$$

where  $E_{\text{homo}}$  is the field amplitude of a homogeneous thin-film emitter with the same FM/NM heterostructure measured under the same experimental conditions (see Sec. S4 in the [Supplementary Material](#)). These results were obtained under an optimum  $\theta_{\text{H}}$ , which yields balanced field amplitudes of the two orthogonal polarizations, thus leading to the highest  $\langle \epsilon \rangle$  under a specific metasurface geometry [same for Fig. 3(a); see Sec. S9 in the [Supplementary Material](#)]. The numerical simulations exhibit good agreement with these results for a wide range of  $d$  [dashed lines in Fig. 3(c)]. We find that elliptically polarized terahertz waves can be generally produced from the spintronic-metasurface devices with  $d < 80 \mu\text{m}$ , while the field circularity monotonically declines as  $d$  increases. In our experiments,  $\langle \epsilon \rangle$  as high as 0.75 can be achieved in the narrow stripes ( $d = 3$  to  $10 \mu\text{m}$ ). Since, with these narrow stripes, the phase difference can stay close to  $\pi/2$  over a broad spectral range [Fig. 2(e)], the ellipticity limit is thus caused by the difference in the spectral amplitudes, which results from the blueshift of the  $E^{\perp}$  spectrum relative to  $E^{\parallel}$  [Fig. 2(d)]. Owing to the strong transverse confinement of these narrow stripes, the corresponding terahertz intensity is, however, generally one order of magnitude lower compared to that from a homogeneous thin film. For wider stripes,  $\eta$  increases, while  $\langle \epsilon \rangle$  decreases because the geometric confinement becomes weaker in the perpendicular direction, which leads to the terahertz emission appearing more alike to that from a homogeneous thin film. Considering both  $\langle \epsilon \rangle$  and the terahertz field strength, the metasurface with  $d \approx 20 \mu\text{m}$  could be the optimum choice, since elliptically polarized terahertz waves with  $\langle \epsilon \rangle \sim 0.6$  can be generated with a relative high intensity of  $\eta \sim 30\%$ . In Fig. 3(d), we further plot the spectrally resolved ellipticity  $\epsilon(\omega)$  and find that high ellipticity of terahertz waveform ( $\epsilon > 0.85$ ) can be realized in a narrow bandwidth between 1.5 and 2 THz when  $d = 3$  to  $10 \mu\text{m}$ . With appropriate spectral filtering, terahertz waveforms with high ellipticity can be generated.

In Fig. 3(d), we can also observe stepwise drops of  $\epsilon(\omega)$  beyond specific resonant frequencies (open symbols), which can be attributed to the collective coupling dynamics between the transient charges and currents over the entire metasurface [see Figs. 1(b) and 1(c)]. In Figs. 4(a) and 4(b), we plot the spectral amplitudes of  $E^{\perp}$  and  $E^{\parallel}$ , respectively, normalized by  $E_{\text{homo}}$ . As shown in Fig. 4(a), the amplitude of  $E^{\perp}$  increases linearly as a function of the terahertz frequency at low frequencies, which is consistent with our geometric-confinement model. Furthermore, multiple spectral anomalies can be observed, manifested as peaks and steps in the normalized spectra, as well as the sharp deviations of the relative phase  $|\varphi^{\perp} - \varphi^{\parallel}|$  from  $\pi/2$  (see Fig. S7 in the [Supplementary Material](#)). Both the spectral and phase variations at the spectral anomalies are responsible for the plummets of field ellipticity, as labeled in Fig. 3(d). These anomaly features can be mostly well reproduced by the

numerical simulations [see Figs. 4(c) and 4(d)], whereas the high-frequency dips present in the simulation for  $E^{\parallel}$  spectra [see Fig. 4(d)] are too weak to be observed experimentally.

In Fig. 4(e), we summarize the anomaly frequencies ( $f_a^m$ ,  $m = 1, 2$  denotes the low- and high-frequency anomalies) for different metasurface periods ( $d + l$ ). Here, we also include the results obtained from FF  $\neq 0.5$  (colored symbols) and those from the emitters with an  $\text{Al}_2\text{O}_3$  substrate (half-filled symbols) (see Sec. S6 and S7 in the [Supplementary Material](#)). Interestingly,  $f_a^m$  is only related to the geometrical period of the metasurface, which can be characterized by a geometrical frequency  $f_{\text{geo}} = v_c / (d + l)$ , where  $v_c$  is the speed of light in vacuum. This indicates that these anomalies originate from the collective dynamics across the entire metasurface. As shown in Fig. 4(e), we find that the low- and high-frequency anomalies can be well fitted by  $f_a^m = \frac{f_{\text{geo}}}{n}$ , where  $n$  is the refractive index of the media. For the high-frequency anomalies  $f_a^2$  (open symbols), the refractive index of the air ( $n_{\text{air}}$ ) yields an excellent fit, while the low-frequency anomalies  $f_a^1$  (filled symbols) can be fitted by the terahertz refractive indices of the substrates ( $n_{\text{SiO}_2} \approx 1.95$  or  $n_{\text{Al}_2\text{O}_3} \approx 3.07^{52}$ ), indicating that it originates from the dynamical coupling through the substrate layer. The different shapes of the anomaly features could be attributed to the Fano-like coupling between the narrow-band Rayleigh diffraction anomaly and the broad-band surface plasmon excitation, which is different for the TE and TM polarizations.<sup>53,54</sup>

With the help of the numerical simulations, we try to better understand the generation mechanism for chiral terahertz waves in the sub-wavelength scale. Taking  $d = 50 \mu\text{m}$  and FF = 0.5 as an example, we plot in Figs. 4(f) and 4(g) the space- and frequency-distributions of the total current density  $|j_a^{\parallel, \perp}|$  in a single metal stripe, which is normalized by the amplitude of the driving current density  $|j_c|$ . For  $j_a^{\parallel}$  [see Fig. 4(g)], the skin effect can be clearly observed, and the current density is largest near the stripe boundaries ( $y = \pm 25 \mu\text{m}$ ). On the contrary, the current density of  $j_a^{\perp}$  [see Fig. 4(f)] is almost completely suppressed at the boundaries due to the conductivity discontinuity, forming a standing-wave-like current distribution across the stripe. Indeed, the appearance of an additional node, which corresponds to a higher-order standing wave, starts to appear when the frequency is higher than  $v_c / 2d$  ( $\sim 3$  THz in this case). In the low-frequency region,  $j_a^{\perp}$  is almost completely subdued throughout the entire stripe, which is consistent with the geometric-confinement model. This can be understood by the fact that more transient charges ( $Q_i$ ) tend to be accumulated at the boundaries when the frequency is lower, leading to a stronger counteractive current ( $j_i$ ), which suppresses the flowing of  $j_a^{\perp}$ . This observation confirms that the spatial confinement on the laser-induced transient currents in the stripe-patterned metasurface is responsible for the observed spectral and phase modulations, as well as for the generation of chiral terahertz waveforms. The spectral anomalies in Figs. 4(a)–4(d) can also be clearly resolved as the sharp peaks or steps of the current density in Figs. 4(f) and 4(g) at the corresponding frequencies.

## 4 Discussion

To increase the generation efficiency of the chiral terahertz waves, an intuitive way is to increase FF for a narrow  $d$  by reducing  $l$ . However, our results indicate that the ellipticity can be deteriorated due to the stronger dynamical coupling between the stripes and the appearance of the spectral anomalies. In Fig. 5(a), we show that  $\langle \epsilon \rangle$  for  $d = 50 \mu\text{m}$  on a  $\text{SiO}_2$  substrate

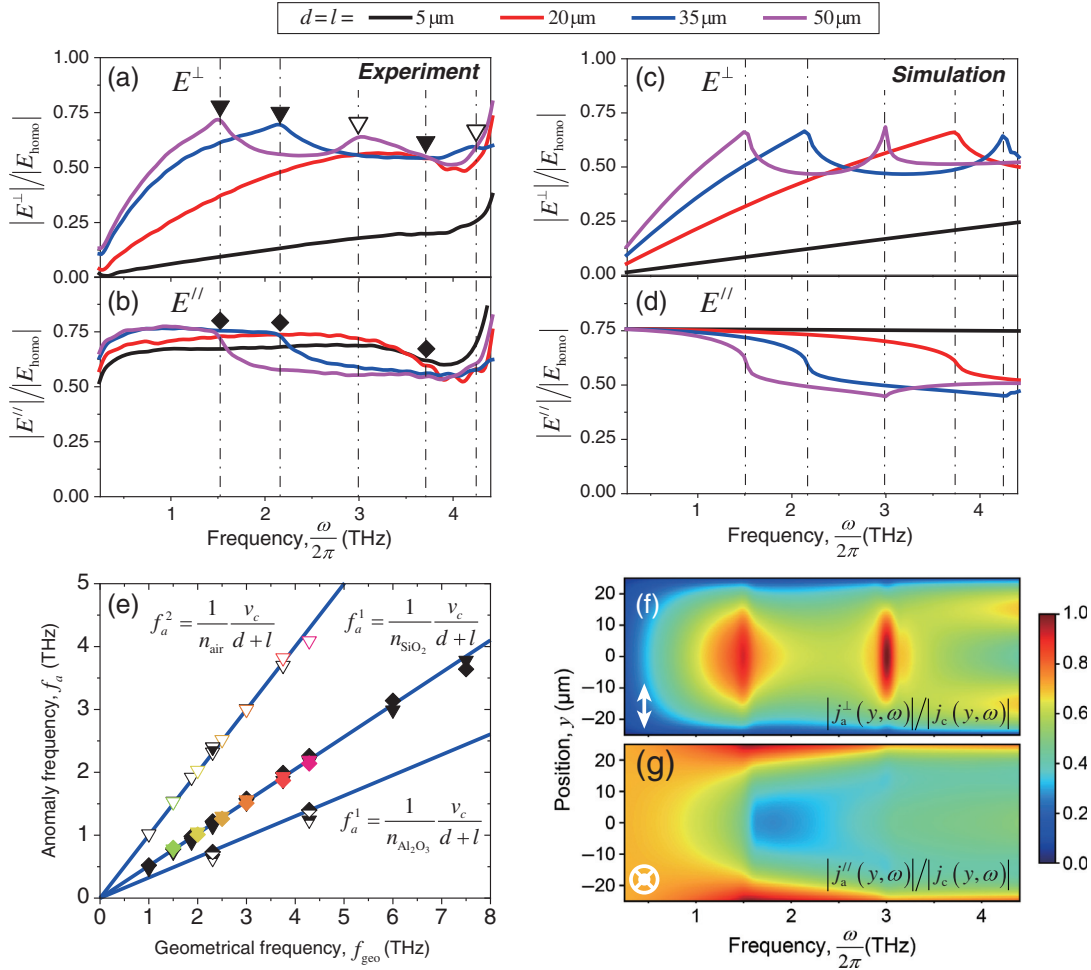


**Fig. 4** Spectral anomaly due to coupling over the metasurface structure. (a) The normalized field spectra of  $E^\perp$  for different  $d$  and  $l$  on a  $\text{SiO}_2$  substrate measured in experiments. The spectra are normalized by those obtained from homogeneous thin-film emitters ( $E_{\text{homo}}$ ). The solid triangles label the low-frequency anomaly features, and the open triangles label the high-frequency ones. (b) Same as (a) for  $E^\parallel$ . The solid diamonds label the corresponding low-frequency anomaly features. (c) and (d) Simulation results obtained under the same conditions as in (a) and (b). The dash-dot lines align the corresponding anomaly features shared by  $E^\parallel$  and  $E^\perp$  spectra. (e) The summary of the anomaly frequencies under different  $d$  and  $l$  as a function of the geometrical frequency  $f_{\text{geo}} = v_c/(d+l)$ . The black filled triangles and diamonds represent the low-frequency features of  $E^\perp$  and  $E^\parallel$ , respectively, for  $\text{FF} = 0.5$  [shown in (a) and (b)]. The black open triangles represent the high-frequency features of  $E^\perp$  for  $\text{FF} = 0.5$ . The colored filled and open symbols are obtained from experiments with  $\text{FF} \neq 0.5$ , and the half-filled symbols illustrate anomaly frequencies measured from emitters with an  $\text{Al}_2\text{O}_3$  substrate. The blue solid lines represent the linear fitting of the experimental data. (f) The spatial and frequency distribution of the normalized total current density flowing perpendicularly to the stripes  $j_a^\perp$  (along the  $y$  axis) for  $d = l = 50 \mu\text{m}$ . The flowing direction of the currents is labeled at the corner. (g) Same as (f) for  $j_a^\parallel$  (along the  $x$  axis).

decreases monotonically when  $\text{FF} > 0.4$ . This can be explained by a stronger capacitive coupling between the stripes [see Fig. 1(c)], which results in weaker  $j_i$  and, hence, less confinement of the transverse currents (see Sec. S8 in the [Supplementary Material](#)). This is supported by the simulation results of the geometrical factor  $C$ , which rises monotonically when the stripes become denser [see Fig. 5(a)]. On the other hand,  $\langle \epsilon \rangle$  does not keep increasing for a lower  $\text{FF}$  as the stripes become more isolated. We find that this could be influenced by the

appearance of the low-frequency anomalies ( $f_a^1$ ) around the spectral peaks of the terahertz waves. Figure 5(c) shows the broadband ellipticity  $\langle \epsilon \rangle$  obtained from our simulation under different  $d$  and  $\text{FF}$ s, the selected cuts of which generally agree with our experimental results [see Figs. 5(a) and 5(b)]. Notably, a high  $\langle \epsilon \rangle$  region exists in between  $\text{FF}=0.3-0.4$  for a number of different  $d$ . Given that the central frequency of the terahertz wave in our experiments is  $\sim 1.5$  THz [Fig. 2(d)], and also the low-frequency anomaly is given by  $f_a^1 = \frac{1}{n_{\text{SiO}_2}} \frac{v_c}{d+l}$  when

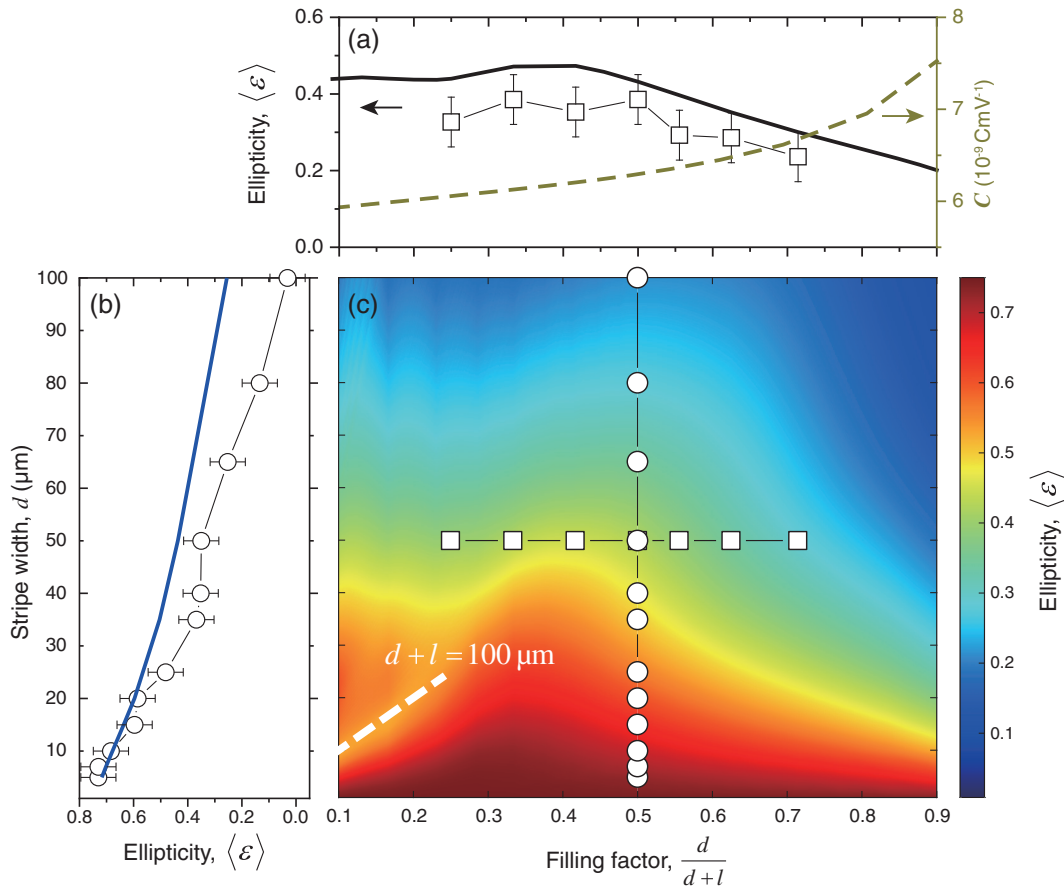


**Fig. 5** Optimizing the terahertz ellipticity of the stripe-patterned metasurface emitter. (a) The broadband ellipticity  $\langle \varepsilon \rangle$  for  $d = 50 \mu\text{m}$  as a function of the FF. The solid line is the simulation results. The simulation results of the geometrical factor  $C$  as a function of FF are shown as the dashed line. (b)  $\langle \varepsilon \rangle$  for FF = 0.5 as a function of the stripe width  $d$ . The solid blue line is the simulation results. (c) 2D map of  $\langle \varepsilon \rangle$  under different FFs and  $d$ . The open symbols label the experimental results in (a) and (b). The dashed line corresponds to  $d + l = 100 \mu\text{m}$ , where the values of anomaly frequency and the terahertz central frequency coincide.

the substrate is  $\text{SiO}_2$ , the agreement of these two frequencies yields  $d + l = 100 \mu\text{m}$ , which shows good correspondence with the left boundary for this high  $\langle \varepsilon \rangle$  region [the white dashed line in Fig. 5(c)]. This result indicates that the coincidence of the value between the anomaly frequency and the terahertz central frequency could reduce  $\langle \varepsilon \rangle$ . As a result, to optimize the field ellipticity under this situation, one should try to increase the anomaly frequencies beyond the spectral range of interest, which could be realized by choosing a substrate with a low terahertz refractive index in practice.

The spintronic-metasurface emitter in our work represents a high-efficiency, flexible, and economical solution for generating broadband chiral terahertz radiations with high ellipticity and a tunable azimuthal angle. First of all, its generation efficiency is comparable to the standard terahertz emitters that are commercially available (see Sec. S4 in the [Supplementary Material](#)). Considering that a peak field strength up to  $300 \text{ kV cm}^{-1}$  can be generated from a homogeneous thin-film emitter when excited by a multi-millijoule laser amplifier,<sup>42</sup> our approach has the potential to generate chiral terahertz fields up to  $\sim 100 \text{ kV cm}^{-1}$  under similar laser conditions [see Fig. 3(c)]. Second, the same emitting device can be compatible with different types of lasers,

from a compact laser oscillator to a high-energy laser amplifier, highlighting the great flexibility of our method. This is also advantageous over the other chiral terahertz sources enabled by nonlinear frequency-conversion in gas plasmas<sup>10-15</sup> and nonlinear crystals,<sup>17,18</sup> for which the high-energy laser pumping is always in demand. Third, our method yields high ellipticity and a tunable azimuthal angle. Previously, flexible manipulation of chiral terahertz waves from a spintronic emitter with a nonuniform external magnetic field was demonstrated, while the reported ellipticity was low, because of the challenge to generate  $\pi/2$  phase difference by varying the nanofilm thickness.<sup>55</sup> In contrast, the  $\pi/2$  phase difference in our work is naturally the result of the transverse confinement applied by the metasurface, which enables the generation of broadband chiral terahertz waves with high ellipticity. The azimuthal angle of the elliptical terahertz wave can also be easily adjusted with our device by rotating the stripe orientation and the external magnetic field together, with a fixed field angle  $\theta_H$ .

## 5 Conclusion

Our work opens a new pathway to metasurface-tailored spintronic emitters for efficient generation and control of terahertz

waves. The combination of ultrabroadband, efficient spintronic emitters and metasurfaces with predesigned functionality could lead to many more types of emitting devices for different spatial and temporal terahertz waveforms (e.g., vector beams, Airy beams, etc.) Although the laser-induced spintronic dynamics in the individual metasurface units are identical in this work, the sophisticated capability of modern spintronic nanoscale engineering has already allowed the manipulation of magnetization, magnetic anisotropy, and spin-current dynamics in each individual unit. This will offer a new degree of freedom to tailor the functionality of spintronic-metasurface devices, which could potentially lead to arbitrary vector-control of broadband terahertz waves in both space and time.

### Acknowledgments

We thank Jingbo Qi and Guixin Li for technical support and helpful discussion. This work was accomplished at Fudan University. L. Z. acknowledges support from the National Key Research and Development Program of China Grant No. 2017YFA0303504), the National Natural Science Foundation of China (Grant No. 11734007), and the Natural Science Foundation of Shanghai (Grant No. 20JC1414601). Y. W. acknowledges support from the National Natural Science Foundation of China (Grant Nos. 11734006 and 11974079), the National Key Research and Development Program of China (Grant No. 2016YFA0300703), and the Shanghai Municipal Science and Technology Major Project (Grant No. 2019SHZDZX01). Z. T. acknowledges financial support from the National Natural Science Foundation of China (Grant No. 11874121) and the Shanghai Municipal Science and Technology Basic Research Project (Grant No. 19JC1410900). C. T. acknowledges support from the National Natural Science Foundation of China (Grant No. 11874123) and the Shanghai Science and Technology Committee (Grant No. 20ZR1406000). Z. T. also thanks the Alexander von Humboldt Foundation for support.

### References

- B. Ferguson and X. Zhang, "Materials for terahertz science and technology," *Nat. Mater.* **1**(1), 26–33 (2002).
- M. Tonouchi, "Cutting-edge terahertz technology," *Nat. Photonics* **1**(2), 97–105 (2007).
- R. Ulbricht et al., "Carrier dynamics in semiconductors studied with time-resolved terahertz spectroscopy," *Rev. Mod. Phys.* **83**(2), 543–586 (2011).
- T. Kampfrath, K. Tanaka, and K. A. Nelson, "Resonant and non-resonant control over matter and light by intense terahertz transients," *Nat. Photonics* **7**(9), 680–690 (2013).
- M. Liu et al., "Terahertz-field-induced insulator-to-metal transition in vanadium dioxide metamaterial," *Nature* **487**(7407), 345–348 (2012).
- S. Schlauderer et al., "Temporal and spectral fingerprints of ultrafast all-coherent spin switching," *Nature* **569**(7756), 383–387 (2019).
- F. Langer et al., "Lightwave-driven quasiparticle collisions on a subcycle timescale," *Nature* **533**(7602), 225–229 (2016).
- B. Zaks, R. B. Liu, and M. S. Sherwin, "Experimental observation of electron-hole recollisions," *Nature* **483**(7391), 580–583 (2012).
- J. Reimann et al., "Subcycle observation of lightwave-driven Dirac currents in a topological surface band," *Nature* **562**(7727), 396–400 (2018).
- Q. Su et al., "Control of terahertz pulse polarization by two crossing DC fields during femtosecond laser filamentation in air," *J. Opt. Soc. Am. B* **36**(10), G1–G5 (2019).
- W. M. Wang et al., "Tunable circularly polarized terahertz radiation from magnetized gas plasma," *Phys. Rev. Lett.* **114**(25), 253901 (2015).
- X. Lu and X. C. Zhang, "Generation of elliptically polarized terahertz waves from laser-induced plasma with double helix electrodes," *Phys. Rev. Lett.* **108**(12), 123903 (2012).
- A. Houard et al., "Strong enhancement of terahertz radiation from laser filaments in air by a static electric field," *Phys. Rev. Lett.* **100**(25), 255006 (2008).
- J. Dai, N. Karpowicz, and X. C. Zhang, "Coherent polarization control of terahertz waves generated from two-color laser-induced gas plasma," *Phys. Rev. Lett.* **103**(2), 023001 (2009).
- Z. Zhang et al., "Manipulation of polarizations for broadband terahertz waves emitted from laser plasma filaments," *Nat. Photonics* **12**(9), 554–559 (2018).
- N. Amer et al., "Generation of terahertz pulses with arbitrary elliptical polarization," *Appl. Phys. Lett.* **87**(22), 221111 (2005).
- M. Sato et al., "Terahertz polarization pulse shaping with arbitrary field control," *Nat. Photonics* **7**(9), 724–731 (2013).
- N. Kanda et al., "The vectorial control of magnetization by light," *Nat. Commun.* **2**, 362 (2011).
- H. Zhao et al., "Generation and manipulation of chiral terahertz waves in the three-dimensional topological insulator Bi<sub>2</sub>Te<sub>3</sub>," *Adv. Photonics* **2**(6), 066003 (2020).
- Y. Gao et al., "Chiral terahertz wave emission from the Weyl semimetal TaAs," *Nat. Commun.* **11**(1), 720 (2020).
- A. Ferrar, et al., "Flexible terahertz wire grid polarizer with high extinction ratio and low loss," *Opt. Lett.* **41**(9), 2009–2012 (2016).
- J. Shan, J. I. Dadap, and T. F. Heinz, "Circularly polarized light in the single-cycle limit: the nature of highly polychromatic radiation of defined polarization," *Opt. Express* **17**(9), 7431–7439 (2009).
- J. Masson and G. Gallot, "Terahertz achromatic quarter-wave plate," *Opt. Lett.* **31**(2), 265–267 (2006).
- X. Cai et al., "Dynamically controlling terahertz wavefronts with cascaded metasurfaces," *Adv. Photonics* **3**(3), 036003 (2021).
- L. Cong et al., "All-optical active THz metasurfaces for ultrafast polarization switching and dynamic beam splitting," *Light Sci. Appl.* **7**(1), 28 (2018).
- N. K. Grady et al., "Terahertz metamaterials for linear polarization conversion and anomalous refraction," *Science* **340**(6138), 1304–1307 (2013).
- M. Jia et al., "Efficient manipulations of circularly polarized terahertz waves with transmissive metasurfaces," *Light Sci. Appl.* **8**(1), 16 (2019).
- T. T. Kim et al., "Electrical access to critical coupling of circularly polarized waves in graphene chiral metamaterials," *Sci. Adv.* **3**(9), e1701377 (2017).
- M. Liu et al., "Temperature-controlled optical activity and negative refractive index," *Adv. Funct. Mater.* **31**(14), 2010249 (2021).
- J. B. Pendry, D. Schurig, and D. R. Smith, "Controlling electromagnetic fields," *Science* **312**(5781), 1780–1782 (2006).
- H.-H. Hsiao, C. H. Chu, and D. P. Tsai, "Fundamentals and applications of metasurfaces," *Small Methods* **1**(4), 1600064 (2017).
- Q. He et al., "High-efficiency metasurfaces: principles, realizations, and applications," *Adv. Opt. Mater.* **6**(19), 1800415 (2018).
- L. Luo et al., "Broadband terahertz generation from metamaterials," *Nat. Commun.* **5**(1), 3055 (2014).
- G. Li, S. Zhang, and T. Zentgraf, "Nonlinear photonic metasurfaces," *Nat. Rev. Mater.* **2**, 17010 (2017).
- C. McDonnell et al., "Functional THz emitters based on Pancharatnam-Berry phase nonlinear metasurfaces," *Nat. Commun.* **12**, 30 (2021).
- T. Seifert et al., "Efficient metallic spintronic emitters of ultrabroadband terahertz radiation," *Nat. Photonics* **10**(7), 483–488 (2016).

37. T. Kampfrath et al., “Terahertz spin current pulses controlled by magnetic heterostructures,” *Nat. Nanotechnol.* **8**(4), 256–260 (2013).
38. D. Yang et al., “Powerful and tunable THz emitters based on the Fe/Pt magnetic heterostructure,” *Adv. Opt. Mater.* **4**(12), 1944–1949 (2016).
39. Y. Wu et al., “High-performance THz emitters based on ferromagnetic/nonmagnetic heterostructures,” *Adv. Mater.* **29**(4), 1603031 (2017).
40. G. Torosyan et al., “Optimized spintronic terahertz emitters based on epitaxial grown Fe/Pt layer structures,” *Sci. Rep.* **8**(1), 1311 (2018).
41. M. Chen et al., “Current-enhanced broadband THz emission from spintronic devices,” *Adv. Opt. Mater.* **7**(4), 1801608 (2019).
42. T. Seifert et al., “Ultrabroadband single-cycle terahertz pulses with peak fields of 300 kV cm<sup>-1</sup> from a metallic spintronic emitter,” *Appl. Phys. Lett.* **110**(25), 252402 (2017).
43. S. Zhang et al., “Solitary beam propagation in periodic layered Kerr media enables high-efficiency pulse compression and mode self-cleaning,” *Light Sci. Appl.* **10**(1), 53 (2021).
44. P. C. M. Planken et al., “Measurement and calculation of the orientation dependence of terahertz pulse detection in ZnTe,” *J. Opt. Soc. Am. B* **18**(3), 313–317 (2001).
45. Q. Wu and X. C. Zhang, “Free-space electro-optic sampling of terahertz beams,” *Appl. Phys. Lett.* **67**(24), 3523–3525 (1995).
46. A. Leitenstorfer et al., “Detectors and sources for ultrabroadband electro-optic sampling: experiment and theory,” *Appl. Phys. Lett.* **74**(11), 1516–1518 (1999).
47. Z. Jin et al., “Terahertz radiation modulated by confinement of picosecond current based on patterned ferromagnetic heterostructures,” *Phys. Status Solidi* **13**(9), 1900057 (2019).
48. L. Nadvorník et al., “Broadband terahertz probes of anisotropic magnetoresistance disentangle extrinsic and intrinsic contributions,” *Phys. Rev. X* **11**, 021031 (2020).
49. COMSOL, <https://www.comsol.com/>.
50. P. Antoine et al., “Polarization of high-order harmonics,” *Phys. Rev. A* **55**(2), 1314–1324 (1997).
51. A. Fleischer et al., “Spin angular momentum and tunable polarization in high-harmonic generation,” *Nat. Photonics* **8**(7), 543–549 (2014).
52. E. D. Palik, *Handbook of Optical Constants of Solids*, Vol. 3, Academic Press, Cambridge, Massachusetts (1998).
53. F. Liu and X. Zhang, “Fano coupling between Rayleigh anomaly and localized surface plasmon resonance for sensor applications,” *Biosens. Bioelectron.* **68**, 719–725 (2015).
54. S. Savoia et al., “Surface sensitivity of Rayleigh anomalies in metallic nanogratings,” *Opt. Express* **21**(20), 23531–23542 (2013).
55. D. Kong et al., “Broadband spintronic terahertz emitter with magnetic-field manipulated polarizations,” *Adv. Opt. Mater.* **7**(20), 1900487 (2019).
56. T. S. Seifert et al., “Terahertz spectroscopy for all-optical spintronic characterization of the spin-Hall-effect metals Pt, W and Cu<sub>80</sub>Ir<sub>20</sub>,” *J. Phys. D.* **51**(36), 364003 (2018).

**Chuanshan Tian** is a professor in the Department of Physics and State Key Laboratory of Surface Physics at Fudan University. He leads a research group devoting to experimental study of exotic phenomena at surfaces and interfaces, with special interest in the development of advanced nonlinear optical spectroscopic techniques to resolve molecular and electronic structure at the interfaces that are relevant to renewable energy and environmental issues.

**Lei Zhou** is a “Xi-De” chair professor and chair of the Department of Physics at Fudan University. He works in the field of nanophotonics, was elected as an OSA Fellow in 2019, and won the second prize of National Natural Science of China in 2019. He is a funding co-editor-in-chief of *Photonics Insights*, a managing editor of *Nanophotonics*, and serves on the editorial board *Physical Review Materials and EPJ Applied Metamaterials*.

**Yizheng Wu** is a professor in the Department of Physics and State Key Laboratory of Surface Physics at Fudan University since 2005. His research interests span over several branches of magnetism and spintronics, including thin film magnetism, antiferromagnetic spintronics, spintronics THz emission and spin-dependent transport in single crystal system.

**Zhensheng Tao** is a professor in the Department of Physics and State Key Laboratory of Surface Physics at Fudan University since 2018. His research activity is devoted to experimental research in optics and condensed matter physics, with particular interest in ultrafast non-equilibrium light-matter interaction and the development of ultrafast technologies.

Biographies of the other authors are not available.